

# Domain decomposition dynamical low-rank for multi-dimensional radiative transfer equations

Stefan Brunner<sup>1</sup>, Lukas Einkemmer<sup>1</sup>, and Terry Haut<sup>2</sup>

<sup>1</sup>*Department of Mathematics, University of Innsbruck, Austria*

<sup>2</sup>*Lawrence Livermore National Laboratory, USA*

January 21, 2026

## Abstract

In this paper, we propose a domain decomposition dynamical low-rank method to solve high-dimensional radiative transfer problems and similar kinetic equations. The algorithm uses a separate low-rank approximation on each spatial subdomain, which means that, for a given accuracy, we can often use a smaller overall rank compared to classic dynamical low-rank methods. In particular, we can solve problems with point sources efficiently, that for classic algorithms require almost full rank. Our algorithm only transfers boundary data between subdomains and is thus very attractive for distributed memory parallelization, where classic dynamical low-rank algorithms suffer from global data dependency. We demonstrate the efficiency of our algorithm by a number of challenging test examples that have both very optical thin and thick regions.

## 1 Introduction

Accurately simulating radiation transport phenomena is vital in many fields. For example, in inertial confinement fusion, atmospheric science and astrophysics. Radiation transport can be described mathematically by the radiative transfer equation (RTE). It models the movement of particles through physical materials, taking absorption, emission and scattering processes into account. Since the distribution of the radiation intensity depends on phase space, i.e. on both spatial and angular variables, we have a high-dimensional problem whose numerical solution suffers from the curse of dimensionality. Thus, finding an efficient solver is difficult.

Commonly, numerical methods based on a phase space discretization are used. This includes the discrete ordinates method (called  $S_N$ ), which evaluates the distribution function pointwise, and methods based on variants of spherical harmonics in velocity space (called  $P_N$ ), i.e. methods which expand the velocity distribution in a global basis. Both methods do suffer from the curse of dimensionality. That is, the number of degrees of freedom scales unfavorable for higher dimensional problems. Another approach, which has also been widely used, are implicit Monte Carlo methods. This approach is based on repeated random sampling of particle trajectories in order to obtain an estimate of the solution. While convergence is technically not dimension dependent, it is usually very slow (square root in the number of particles). Thus, usually this approach also comes with high computational cost, especially for problems with regions that are optically thick. For more details we refer the reader to, e.g., [3].

Recently, dynamical low-rank approximations (DLRA) have seen increasing interest for kinetic problems in general and radiation transport more specifically (see, e.g., the review article [19]). The main idea is to approximate the distribution function using lower dimensional low-rank factors that only depend on either space or angular variables, thereby significantly reducing memory and computational cost. For these low-rank factors, (partial differential) equations of motions are then derived that can be solved numerically. Some early work on the radiative transfer equation can be found in [31, 11, 15] and applications such as radiation therapy [26] have been pursued. In addition, much work in recent years has resulted in conservative variants of these schemes (see, e.g., [16, 10, 21, 30]) and (implicit or semi-implicit) schemes that preserve the underlying diffusive or fluid limit of the kinetic equation (see, e.g., [15, 14, 20]).

Dynamical low-rank methods can be extremely effective for such problems and often result in drastically reduced memory and computational cost. This is particularly true on modern computing architectures, such as graphic processing units (GPUs; see [4]). However, the dynamical low-rank approach fundamentally uses an approximation with global basis functions. This results in global data dependency, which is undesirable when parallelizing such methods to distributed memory supercomputers. Moreover, there are some problems where there is no global low-rank structure (e.g. a point source). In this case classic low-rank methods do require a large rank to obtain accurate results.

In this paper, we propose a domain decomposition dynamical low-rank approach that uses a separate low-rank approximation on each subdomain. In particular,

- the method only exchanges boundary data between subdomains. That is, there is only local data dependency between subdomains;
- since we have a low-rank approximation on each subdomain, we can solve problems that are of high rank locally and problems, which have parts of the domain where the rank is low (e.g. due to strong absorption), much more efficiently than classic dynamical low-rank methods.

As we will see, a main difficulty is to obtain a domain decomposition method that does not suffer from excessive increase of rank in intermediate steps (which would increase memory cost and decrease computational efficiency significantly). Our approach, which is based on the projector splitting integrator, requires some augmentation but not more so than classic Basis Update and Galerkin (BUG) integrators (see, e.g., [6]).

As related work, we mention [29], where the authors decompose the angular domain into multiple parts and apply DLRA to each of those parts separately. This is an easier problem, because if the subdomains are chosen as quadrants/octants of angular space, no coupling between the subdomains is necessary. However, the approach is also more limiting since usually much more grid points are used in the spatial domain and there is thus more potential for parallelization. Moreover, different parts in the spatial domain can behave very differently. For example, in inertial confinement fusion it is very common to have parts of the domain which are very optically thick and are thus close to the diffusion limit. Such regions can be represented easily with a very low rank. Our spatial domain decomposition approach can easily exploit such a structure of the problem. The approach of [29], on the other hand, would still require a low-rank approximation that is global in the spatial variables.

We also mention [24], which proposes a low-rank approximation that treats inflow/outflow boundary conditions. While the authors do not directly consider domain decomposition in their work, the problem of imposing inflow/outflow boundary conditions is very much related to our approach, which only communicates boundary information between two subdomains.

The remainder of the paper is structured as follows. In section 2, we introduce our model of the radiative transfer equation and give a short recap of how classic dynamical low-rank methods are used in that context. In section 3, we present the proposed domain decomposition algorithm. Finally, in section 4, we show numerical results for some known test problems, comparing our new algorithm with the classic DLRA approach.

## 2 Dynamical low-rank approximation of the radiative transfer equation

In this paper we consider the following  $2 \times 1$  dimensional radiative transfer equation (see, e.g., [3])

$$\begin{aligned} \partial_t f(t, x, y, \phi) + c_{\text{adv}} v \cdot \nabla_{x,y} f(t, x, y, \phi) \\ = c_s(x, y) \frac{1}{2\pi} \rho(t, x, y) - c_t(x, y) f(t, x, y, \phi) + Q(x, y), \end{aligned} \quad (1)$$

where  $(x, y) \in \Omega = [0, 1] \times [0, 1]$ , the angle  $\phi \in [0, 2\pi]$  and  $f : \mathbb{R}^+ \times \Omega \times [0, 2\pi] \rightarrow \mathbb{R}^+$  is the distribution function. It describes the radiation energy density flowing in a particular direction specified by the angle  $\phi$ . The velocity  $v$  is given by  $v = (\cos \phi, \sin \phi)$ . The coefficient  $c_{\text{adv}}$  is the advection speed, which is equal to the value of the speed of light in the chosen unit system. The other coefficients,  $c_s$  and  $c_t$ , are the scattering and the total coefficients. The total coefficient is defined as the sum of the absorption and scattering coefficient, i.e.  $c_t = c_a + c_s$ . Lastly,  $Q$  is an external source term.

The most important physical observable is the density  $\rho$ , which can be computed from the distribution function as follows

$$\rho(t, x, y) = \int f(t, x, y, \phi) d\phi = \langle f \rangle_\phi.$$

Due to the high dimensionality of the problem, we want to approximate the distribution function  $f(t, x, y, \phi)$  by a low-rank approximation

$$f(t, x, y, \phi) = \sum_{i,j=1}^r U_i(t, x, y) S_{ij}(t) V_j(t, \phi). \quad (2)$$

Note that this is similar to a singular value decomposition (SVD), but formulated here in the continuous setting. The functions  $U_i$ ,  $S_{ij}$  and  $V_j$  are the low-rank factors and satisfy the orthonormality conditions  $\langle U_i, U_k \rangle_{x,y} = \delta_{ik}$  and  $\langle V_j, V_l \rangle_\phi = \delta_{jl}$ , where  $\langle \cdot, \cdot \rangle$  denotes the standard  $L^2$  inner product. From now on we will denote sums starting at index 1 and ending at index  $r$  simply by  $\sum_{i,j}$ , meaning we only write the summation indices but not the bounds.

Following [25, 18], a system of evolution equations for the low-rank factors can be derived. The resulting system, however, is ill-conditioned in the presence of small singular values. To avoid this problem so-called robust integrators have been developed. The most common ones are the projector splitting integrator (PSI) [28, 18] and the basis update and Galerkin integrator (BUG) [7, 6], but also a parallel integrator [5] has been proposed.

In this work we focus, for reasons that will be explained in more detail later, on the projector splitting integrator. The PSI splits the projector onto the tangent space of the low-rank manifold into three parts corresponding to the three low-rank factors. We will now summarize the method (for more details, see [7, 18, 28]). First, we write equation (1) as follows

$$\partial_t f = F(f), \quad F(f) = -c_{\text{adv}} v \cdot \nabla_{x,y} f + c_s \frac{1}{2\pi} \rho - c_t f + Q. \quad (3)$$

Starting with a low-rank representation at time  $t_n$

$$f^n(x, y, \phi) = \sum_{i,j} U_i^n(x, y) S_{ij}^n V_j^n(\phi),$$

the (first order) PSI proceeds as follows:

1. **K-step:** Integrate from  $t_n$  to  $t_{n+1}$  the differential equation

$$\partial_t K_j(t, x, y) = \left\langle V_j^n(\phi), F \left( \sum_k K_k(t, x, y) V_k^n(\phi) \right) \right\rangle_\phi, \quad (4)$$

$$K_j(t_n, x, y) = \sum_i U_i^n(x, y) S_{ij}^n,$$

to obtain  $K_j^{n+1}(x, y) = K_j(t_{n+1}, x, y)$ . For the space spanned by the functions  $K_j^{n+1}(x, y)$  for  $j \in \{1, \dots, r\}$ , compute an orthonormal basis (e.g. by a QR decomposition)  $U_i^{n+1}(x, y)$  for  $i \in \{1, \dots, r\}$ , such that  $K_j^{n+1}(x, y) = \sum_i U_i^{n+1}(x, y) \hat{S}_{ij}$ .

2. **S-step:** Integrate from  $t_n$  to  $t_{n+1}$  the differential equation

$$\partial_t S_{ij}(t) = - \left\langle U_i^{n+1}(x, y) V_j^n(\phi), F \left( \sum_{k,l} U_l^{n+1}(x, y) S_{lk}(t) V_k^n(\phi) \right) \right\rangle_{x,y,\phi}, \quad (5)$$

$$S_{ij}(t_n) = \hat{S}_{ij}.$$

Set  $\tilde{S}_{ij} = S_{ij}(t_{n+1})$ .

3. **L-step:** Integrate from  $t_n$  to  $t_{n+1}$  the differential equation

$$\partial_t L_i(t, \phi) = \left\langle U_i^{n+1}(x, y), F \left( \sum_l U_l^{n+1}(x, y) L_l(t, \phi) \right) \right\rangle_{x,y}, \quad (6)$$

$$L_i(t_n, \phi) = \sum_j V_j^n(\phi) \tilde{S}_{ij},$$

to obtain  $L_i^{n+1}(\phi) = L(t_{n+1}, \phi)$ . For the space spanned by the functions  $L_i^{n+1}(\phi)$  for  $i \in \{1, \dots, r\}$ , compute an orthonormal basis  $V_j^{n+1}(\phi)$  for  $j \in \{1, \dots, r\}$ , such that  $L_i^{n+1}(\phi) = \sum_j V_j^{n+1}(\phi) S_{ij}^{n+1}$ .

The approximation at time  $t_{n+1}$  is then given by

$$f^{n+1}(x, y, \phi) = \sum_{i,j} U_i^{n+1}(x, y) S_{ij}^{n+1} V_j^{n+1}(\phi).$$

Next, apply the projector splitting integrator to the radiative transfer equation (1). For the sake of simplicity, we will omit variable dependency. Plugging equation (3) into equation (4) we get the K step

$$\partial_t K_j = -c_{\text{adv}} \sum_k \langle V_j^n, v V_k^n \rangle_\phi \nabla_{x,y} K_k + c_s \frac{1}{2\pi} \sum_k K_k \langle V_k^n \rangle_\phi \langle V_j^n \rangle_\phi - c_t K_j + Q \langle V_j^n \rangle_\phi. \quad (7)$$

Similarly, we get the evolution equation for the  $S$ -step

$$\begin{aligned}\partial_t S_{ij} = & c_{\text{adv}} \sum_{k,l} \langle U_i^{n+1}, \nabla_{x,y} U_l^{n+1} \rangle_{x,y} \langle V_j^n, v V_k^n \rangle_\phi S_{lk} \\ & - \frac{1}{2\pi} \sum_{k,l} \langle U_i^{n+1}, c_s U_l^{n+1} \rangle_{x,y} \langle V_k^n \rangle_\phi \langle V_j^n \rangle_\phi S_{lk} \\ & + \sum_l \langle U_i^{n+1}, c_t U_l^{n+1} \rangle_{x,y} S_{lj} - \langle U_i^{n+1}, Q \rangle_{x,y} \langle V_j^n \rangle_\phi\end{aligned}\quad (8)$$

and for the  $L$ -step

$$\begin{aligned}\partial_t L_i = & -c_{\text{adv}} \sum_l \langle U_i^{n+1}, \nabla_{x,y} U_l^{n+1} \rangle_{x,y} v L_l + \frac{1}{2\pi} \sum_l \langle U_i^{n+1}, c_s U_l^{n+1} \rangle_{x,y} \langle L_l \rangle_\phi \\ & - \sum_l \langle U_i^{n+1}, c_t U_l^{n+1} \rangle_{x,y} L_l + \langle U_i^{n+1}, Q \rangle_{x,y}.\end{aligned}\quad (9)$$

Note that as  $U$  and  $K$  depend only on spatial variables,  $V$  and  $L$  only depend on the angle, and  $S$  does not depend on either, storing the low-rank factors is much cheaper than storing the entire distribution function. Moreover, equations (7)-(9) can be evaluated efficiently and the computational complexity of doing so scales at most with either the number of spatial grid points or the number of angles (but not the product of both). For a more detailed computational and memory complexity analysis we refer the reader, e.g., to [18].

### 3 Domain decomposition low-rank algorithm

In this section, we describe the proposed algorithm, which combines domain decomposition with the dynamical low-rank approach to solve equation (1). A block based domain decomposition, as illustrated in Figure 1, is considered. Our approach is based on imposing inflow/outflow conditions on each subdomain. That is, the outflow of a neighboring domain becomes the inflow for the current domain and vice versa. Such boundary conditions have already been considered in the context of a steady state problem [24]. An issue here is that potentially new information enters via the boundary as the neighboring subdomain uses a low-rank approximation with, in general, different basis functions. That is, the low-rank approximation does not necessarily have the correct basis to accurately represent the information from the boundary. This was already recognized in [24] and, in fact, a naive algorithm gives incorrect results. The obvious solution is to augment the basis with information from the neighboring domains.

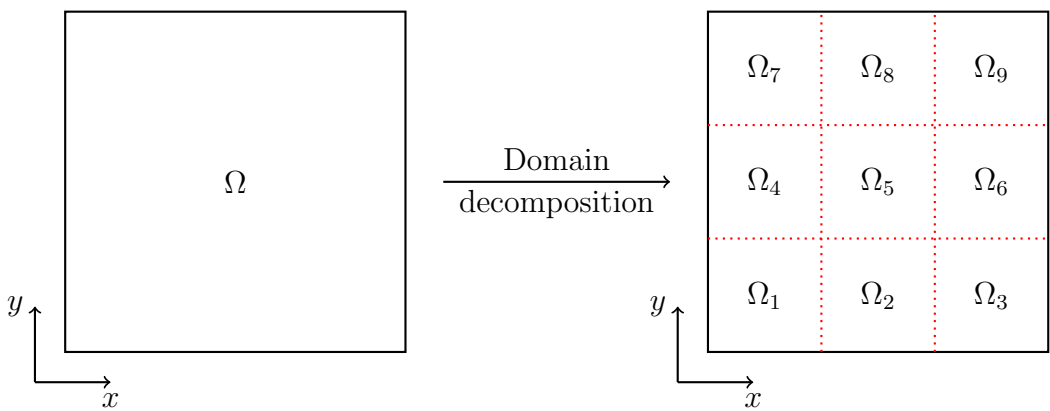


Figure 1: Illustration of block domain decomposition.

However, doing this in a naive way would be very costly as in two dimensions we have potentially eight neighboring subdomains which all, in general, have a distinct low-rank representation. This would increase memory usage drastically and is even worse in terms of computational effort as the computational cost scales with  $r^2$ . We solve this problem in the following way:

- First, we perform a splitting of the advection such that only one-dimensional advects need to be considered. This has the benefit that we only require augmentation by at most two neighboring subdomains in each step of the algorithm. Splitting into different directions is a very common approach for kinetic equations (see, e.g., [9, 34, 12]), although in these works it is done for a somewhat different reason (to avoid the complexity of multi-dimensional interpolation).
- Since there is usually a significant overlap of the information contained in the basis functions of neighboring domains, we add only information that is not redundant. That is, we only add information that is not yet contained in the low-rank representation of the current subdomain.

While, in principle, doing such an augmentation is very natural for the BUG integrators (see, e.g., [6]), doing so would result in a relatively large number of basis functions. The reason for this is that modern BUG integrators have an intrinsic augmentation that needs to be done in addition to the augmentation required by the inflow. The larger the overall space is the more problematic this becomes due to the at least quadratic scaling in rank that holds for all of these methods. Thus, we will focus here on the projector splitting integrator. This allows us to obtain an algorithm (as we will see in the numerical results) that does not need to increase the rank for the intermediate computation to above roughly  $2r$  (i.e. is about the same as for a BUG integrator), where  $r$  is the rank required to store the solution.

In the following we will explain our algorithm in detail for the two-dimensional case. However, due to the splitting the extension to three dimensions is immediate. We start with the radiative transfer equation (1) and treat the  $x$  advection, the  $y$  advection, and the combined absorption, scattering and the source term separately. Using  $v_x = \cos(\phi)$  and  $v_y = \sin(\phi)$  the splitting algorithm to update  $f^n(x, y, \phi)$  to  $f^{n+1}(x, y, \phi)$  reads as follows.

1. We first consider the  $x$  advection:

$$\begin{aligned} \partial_t f(t, x, y, \phi) + c_{\text{adv}} v_x(\phi) \partial_x f(t, x, y, \phi) &= 0, \\ f(t_n, x, y, \phi) &= f^n(x, y, \phi). \end{aligned}$$

By solving this equation we obtain  $f^*(x, y, \phi) = f(t_{n+1}, x, y, \phi)$ .

2. Next, we treat the  $y$  advection:

$$\begin{aligned} \partial_t f(t, x, y, \phi) + c_{\text{adv}} v_y(\phi) \partial_y f(t, x, y, \phi) &= 0, \\ f(t_n, x, y, \phi) &= f^*(x, y, \phi). \end{aligned}$$

By solving the equation we obtain  $f^{**}(x, y, \phi) = f(t_{n+1}, x, y, \phi)$ .

3. Finally, we consider absorption, scattering and the source term:

$$\begin{aligned} \partial_t f(t, x, y, \phi) &= c_s(x, y) \frac{1}{2\pi} \rho(t, x, y) - c_t(x, y) f(t, x, y, \phi) + Q(x, y), \\ f(t_n, x, y, \phi) &= f^{**}(x, y, \phi). \end{aligned}$$

By solving the equation we obtain  $f^{n+1}(x, y, \phi) = f(t_{n+1}, x, y, \phi)$ .

This is first order accurate in time. However, it can easily be raised to second or higher order by the usual splitting techniques (see, e.g., [28, 22]). In the following we apply the projector splitting integrator to each of these three steps separately and discuss how to impose the inflow boundary conditions.

### 3.1 Step 1: DLR advection in $x$

We start with the advection in the  $x$ -direction, i.e. step 1. Similar to section 2 we get

$$\partial_t K_j = -c_{\text{adv}} \sum_k \langle V_j, v_x V_k \rangle_\phi \partial_x K_k, \quad (10)$$

$$\partial_t S_{ij} = c_{\text{adv}} \sum_{k,l} \langle U_i, \partial_x U_l \rangle_{x,y} \langle V_j, v_x V_k \rangle_\phi S_{lk}, \quad (11)$$

$$\partial_t L_i = -c_{\text{adv}} \sum_l \langle U_i, \partial_x U_l \rangle_{x,y} v_x L_l. \quad (12)$$

To solve equation (10) we need boundary information at the inflow boundaries. This data is obtained from the neighboring domains (see illustration in Figure 2). Let  $\Omega_C$  be our current subdomain,  $\Omega_L$  the subdomain to the left and  $\Omega_R$  the subdomain to the right. If  $\phi \leq \frac{\pi}{2}$  or  $\phi \geq \frac{3\pi}{2}$ , then our velocity in the  $x$  direction is  $\cos(\phi) \geq 0$ , and thus we have flow to the right, indicated by the blue arrows. In this case, we have inflow at our left boundary  $\partial\Omega_L$  and outflow on our right boundary  $\partial\Omega_R$ . If, on the other hand,  $\frac{\pi}{2} < \phi < \frac{3\pi}{2}$ , then the velocity in the  $x$  direction is  $\cos(\phi) < 0$ , and we thus have flow to the left, indicated by the green arrows.

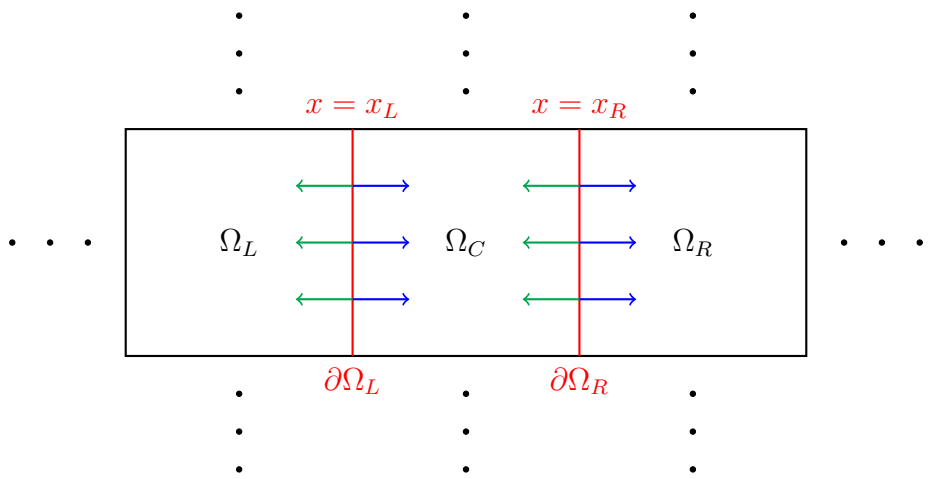


Figure 2: Inflow and outflow for subdomain  $\Omega_C$  during the  $x$  advection step.

We denote the value of  $f$  at the boundary by

$$f^b : \mathbb{R}^+ \times \{x_L, x_R\} \times \Omega_C^Y \times [0, 2\pi) \rightarrow \mathbb{R}^+. \quad (13)$$

We then have on the left boundary

$$f^b(t, x_L, y, \phi) = \begin{cases} f_{\text{in}}(t, x_L, y, \phi), & \text{if } (\phi \leq \frac{\pi}{2}) \vee (\phi \geq \frac{3\pi}{2}), \\ f(t, x_L, y, \phi), & \text{if } \frac{\pi}{2} < \phi < \frac{3\pi}{2}, \end{cases} \quad (14)$$

and on the right boundary

$$f^b(t, x_R, y, \phi) = \begin{cases} f_{\text{in}}(t, x_R, y, \phi), & \text{if } \frac{\pi}{2} < \phi < \frac{3\pi}{2}, \\ f(t, x_R, y, \phi), & \text{if } (\phi \leq \frac{\pi}{2}) \vee (\phi \geq \frac{3\pi}{2}), \end{cases} \quad (15)$$

where  $f_{\text{in}}$  can be obtained by evaluating the low-rank representation of the neighboring sub-domains at  $x_L$  and  $x_R$  (this is the inflow data). At the outflow boundary we simply have the solution provided by the low-rank representation on the current subdomain, i.e.  $f$  evaluated at  $x_L$  and  $x_R$ , respectively.

Our goal, however, is to obtain boundary data for  $K_j$ , not for  $f$ . To accomplish this, we project  $f^b(t, x, y, \phi)$  to the space spanned by the  $V_j$  (as has been done in [24]). That is, for  $x \in \{x_L, x_R\}$  we have

$$K_j^b(t, x, y) = \langle f^b(t, x, y, \phi), V_j(t, \phi) \rangle_\phi.$$

Using equations (14) and (15) we get

$$\begin{aligned} K_j^b(t, x_L, y) &= \left\langle f_{\text{in}}(t, x_L, y, \phi) \mathbb{1}_{(\phi \leq \frac{\pi}{2}) \vee (\phi \geq \frac{3\pi}{2})}, V_j(t, \phi) \right\rangle_\phi \\ &\quad + \left\langle f(t, x_L, y, \phi) \mathbb{1}_{\frac{\pi}{2} < \phi < \frac{3\pi}{2}}, V_j(t, \phi) \right\rangle_\phi \end{aligned}$$

and

$$\begin{aligned} K_j^b(t, x_R, y) &= \left\langle f_{\text{in}}(t, x_R, y, \phi) \mathbb{1}_{\frac{\pi}{2} < \phi < \frac{3\pi}{2}}, V_j(t, \phi) \right\rangle_\phi \\ &\quad + \left\langle f(t, x_R, y, \phi) \mathbb{1}_{(\phi \leq \frac{\pi}{2}) \vee (\phi \geq \frac{3\pi}{2})}, V_j(t, \phi) \right\rangle_\phi. \end{aligned}$$

We can now use the low-rank representation  $f = \sum_l K_l V_l$  for the outflow boundary and the low-rank representations from the two neighboring domains, denoted by  $f^L = \sum_l K_l^L V_l^L$  and  $f^R = \sum_l K_l^R V_l^R$ , respectively, to get

$$\begin{aligned} K_j^b(t, x_L, y) &= \sum_l K_l^L(t, x_L, y) \left\langle \mathbb{1}_{(\phi \leq \frac{\pi}{2}) \vee (\phi \geq \frac{3\pi}{2})} V_l^L(t, \phi), V_j(t, \phi) \right\rangle_\phi \\ &\quad + \sum_l K_l(t, x_L, y) \left\langle \mathbb{1}_{\frac{\pi}{2} < \phi < \frac{3\pi}{2}} V_l(t, \phi), V_j(t, \phi) \right\rangle_\phi \\ K_j^b(t, x_R, y) &= \sum_l K_l^R(t, x_R, y) \left\langle \mathbb{1}_{\frac{\pi}{2} < \phi < \frac{3\pi}{2}} V_l^R(t, \phi), V_j(t, \phi) \right\rangle_\phi \\ &\quad + \sum_l K_l(t, x_R, y) \left\langle \mathbb{1}_{(\phi \leq \frac{\pi}{2}) \vee (\phi \geq \frac{3\pi}{2})} V_l(t, \phi), V_j(t, \phi) \right\rangle_\phi, \end{aligned} \quad (16)$$

Combining the boundary data for  $K$  with equation (10) the K step of the projector splitting integrator for the  $x$  advection is now given by

$$\partial_t K_j = -c_{\text{adv}} \sum_k \langle V_j, v_x V_k \rangle_\phi \partial_x K_k, \quad K_j|_{x \in \{x_L, x_R\}} = K_j^b. \quad (17)$$

We slightly rewrite equation (11) for the S step such that we can directly use the boundary data which are expressed in  $K$  and not in  $U$ . This gives

$$\partial_t S_{ij} = c_{\text{adv}} \sum_k \langle U_i, \partial_x K_k \rangle_{x,y} \langle V_j, v_x V_k \rangle_\phi, \quad K_j|_{x \in \{x_L, x_R\}} = K_j^b. \quad (18)$$

We do the same for the L step, which gives

$$\partial_t L_i = -c_{\text{adv}} \sum_j \langle U_i, \partial_x K_j \rangle_{x,y} v_x V_j, \quad K_j|_{x \in \{x_L, x_R\}} = K_j^b. \quad (19)$$

The corresponding projector splitting integrator for the  $x$  advection is summarized in algorithm 1.

---

**Algorithm 1** Projector splitting algorithm for  $x$  advection.

---

**Input:**  $U_i^0, S_{ij}^0, V_j^0$  (such that  $f^0(x, y, \phi) = \sum_{i,j} U_i^0(x, y) S_{ij}^0 V_j^0(\phi)$ ),  $K_j^{L,0}, V_j^{L,0}, K_j^{R,0}, V_j^{R,0}$

**Output:**  $U_i^1, S_{ij}^3, V_j^1$  (such that  $f^1(x, y, \phi) = \sum_{i,j} U_i^1(x, y) S_{ij}^3 V_j^1(\phi)$ )

- 1: Solve equation (17) with initial value  $\sum_{i,j} U_i^0 S_{ij}^0$  and boundary value  $K_j^b$  up to time  $\Delta t$  to obtain  $K_j^1$ .
- 2: Perform a QR decomposition of  $K_j^1$  to get  $U_i^1$  and  $S_{ij}^1$ .
- 3: Solve equation (18) with initial value  $S_{ij}^1$  and boundary value  $K_j^b$  up to time  $\Delta t$  to obtain  $S_{ij}^2$ .
- 4: Solve equation (19) with initial value  $\sum_j S_{ij}^2 V_j^0$  and boundary value  $K_j^b$  up to time  $\Delta t$  to obtain  $L_i^1$ .
- 5: Perform a QR decomposition of  $L_i^1$  to get  $V_j^1$  and  $S_{ij}^3$ .

The boundary values  $K_j^b$  were calculated as in (16) using the low-rank representations from the neighboring subdomains  $K_j^{L,0}, V_j^{L,0}, K_j^{R,0}$ , and  $V_j^{R,0}$ .

---

### 3.2 Step 2: DLR advection in $y$

The advection in the  $y$  direction proceeds completely analogous to the advection in the  $x$  direction described in the previous section, just that now the inflowing values come from the subdomains on the bottom and the top of our current subdomain. For completeness, we reproduce here the obtained evolution equations for the K step

$$\partial_t K_j = -c_{\text{adv}} \sum_k \langle V_j, v_y V_k \rangle_\phi \partial_y K_k, \quad K_j|_{y \in \{y_B, y_T\}} = K_j^b, \quad (20)$$

S step

$$\partial_t S_{ij} = c_{\text{adv}} \sum_k \langle U_i, \partial_y K_k \rangle_{x,y} \langle V_j, v_y V_k \rangle_\phi, \quad K_j|_{y \in \{y_B, y_T\}} = K_j^b, \quad (21)$$

and L step

$$\partial_t L_i = -c_{\text{adv}} \sum_j \langle U_i, \partial_y K_j \rangle_{x,y} v_y V_j, \quad K_j|_{y \in \{y_B, y_T\}} = K_j^b. \quad (22)$$

The boundary data  $K_j^b$  is computed according to

$$\begin{aligned}
K_j^b(t, x, y_B) &= \sum_l K_l^B(t, x, y_B) \langle \mathbb{1}_{0 \leq \phi \leq \pi} V_j^B(t, \phi), V_j(t, \phi) \rangle_\phi \\
&\quad + \sum_l K_l(t, x, y_B) \langle \mathbb{1}_{\pi < \phi < 2\pi} V_l(t, \phi), V_j(t, \phi) \rangle_\phi \\
K_j^b(t, x, y_T) &= \sum_l K_l^T(t, x, y_T) \langle \mathbb{1}_{\pi < \phi < 2\pi} V_l^T(t, \phi), V_j(t, \phi) \rangle_\phi \\
&\quad + \sum_l K_l(t, x, y_T) \langle \mathbb{1}_{0 \leq \phi \leq \pi} V_l(t, \phi), V_j(t, \phi) \rangle_\phi,
\end{aligned} \tag{23}$$

The corresponding projector splitting integrator for the  $y$  advection is summarized in algorithm 2.

---

**Algorithm 2** Projector splitting algorithm for  $y$  advection.

---

**Input:**  $U_i^0, S_{ij}^0, V_j^0$  (such that  $f^0(x, y, \phi) = \sum_{i,j} U_i^0(x, y) S_{ij}^0 V_j^0(\phi)$ ),  $K_j^{B,0}, V_j^{B,0}, K_j^{T,0}, V_j^{T,0}$

**Output:**  $U_i^1, S_{ij}^3, V_j^1$  (such that  $f^1(x, y, \phi) = \sum_{i,j} U_i^1(x, y) S_{ij}^3 V_j^1(\phi)$ )

- 1: Solve equation (20) with initial value  $\sum_{i,j} U_i^0 S_{ij}^0$  and boundary value  $K_j^b$  up to time  $\Delta t$  to obtain  $K_j^1$ .
- 2: Perform a QR decomposition of  $K_j^1$  to get  $U_i^1$  and  $S_{ij}^1$ .
- 3: Solve equation (21) with initial value  $S_{ij}^1$  and boundary value  $K_j^b$  up to time  $\Delta t$  to obtain  $S_{ij}^2$ .
- 4: Solve equation (22) with initial value  $\sum_j S_{ij}^2 V_j^0$  and boundary value  $K_j^b$  up to time  $\Delta t$  to obtain  $L_i^1$ .
- 5: Perform a QR decomposition of  $L_i^1$  to get  $V_j^1$  and  $S_{ij}^3$ .

The boundary values  $K_j^b$  were calculated as in (23) using the low-rank representations from the neighboring subdomains  $K_j^{B,0}, V_j^{B,0}, K_j^{T,0}$ , and  $V_j^{T,0}$ .

---

### 3.3 Step 3: DLR for absorption, scattering, and the source term

Here we can use a standard projector splitting operator as no boundary information is needed for the spatially pointwise absorption, scattering, and source terms. The equation for the K step is

$$\partial_t K_j = \frac{c_s}{2\pi} \sum_k K_k \langle V_k \rangle_\phi \langle V_j \rangle_\phi - c_t K_j + Q \langle V_j \rangle_\phi. \tag{24}$$

For the S step we get

$$\partial_t S_{ij} = -\frac{1}{2\pi} \sum_{k,l} \langle U_i, c_s U_l \rangle_{x,y} \langle V_k \rangle_\phi \langle V_j \rangle_\phi S_{lk} + \sum_l \langle U_i, c_t U_l \rangle_{x,y} S_{lj} - \langle U_i, Q \rangle_{x,y} \langle V_j \rangle_\phi \tag{25}$$

and finally for the L step we have

$$\partial_t L_i = \frac{1}{2\pi} \sum_l \langle U_i, c_s U_l \rangle_{x,y} \langle L_l \rangle_\phi - \sum_l \langle U_i, c_t U_l \rangle_{x,y} L_l + \langle U_i, Q \rangle_{x,y}. \tag{26}$$

The corresponding projector splitting integrator for absorption, scattering and the source term is summarized in algorithm 3.

---

**Algorithm 3** Projector splitting algorithm for absorption, scattering and the source term.

---

**Input:**  $U_i^0, S_{ij}^0, V_j^0$  (such that  $f^0(x, y, \phi) = \sum_{i,j} U_i^0(x, y) S_{ij}^0 V_j^0(\phi)$ )

**Output:**  $U_i^1, S_{ij}^3, V_j^1$  (such that  $f^1(x, y, \phi) = \sum_{i,j} U_i^1(x, y) S_{ij}^3 V_j^1(\phi)$ )

- 1: Solve equation (24) with initial value  $\sum_{i,j} U_i^0 S_{ij}^0$  up to time  $\Delta t$  to obtain  $K_j^1$ .
- 2: Perform a QR decomposition of  $K_j^1$  to get  $U_i^1$  and  $S_{ij}^1$ .
- 3: Solve equation (25) with initial value  $S_{ij}^1$  up to time  $\Delta t$  to obtain  $S_{ij}^2$ .
- 4: Solve equation (26) with initial value  $\sum_j S_{ij}^2 V_j^0$  up to time  $\Delta t$  to obtain  $L_i^1$ .
- 5: Perform a QR decomposition of  $L_i^1$  to get  $V_j^1$  and  $S_{ij}^3$ .

---

### 3.4 Augmentation and adaptive rank strategy

As mentioned in the beginning of the section, it is not sufficient to simply run the derived algorithm with the obtained boundary data. We also have to ensure that the span of  $V$  is sufficiently rich to accurately represent the boundary data from neighboring domains. To add the relevant information (contained in the  $V$  basis of neighboring domains) is the task of the augmentation step described in this section. Augmentation is now a classic concept for dynamical low-rank methods. It is done in the augmented BUG integrator (as the classic variant without augmentation can be unstable; see, e.g., [13]). In this context it has also been used to get higher order schemes [8] and to enforce conservation [17, 1, 33] or boundary conditions [27]. Augmentation is most commonly encountered for the BUG type integrators, but has also been done for the projector splitting integrator, see, e.g., [24]. A crucial goal in the present context is to augment as few basis functions as necessary in order to keep computational and memory cost as low as possible.

Although, in principle, our augmentation procedure can be done in the continuous case, it is significantly more straightforward to describe it in the language of linear algebra. Thus, from now on we assume that we have already performed a spatial and velocity/angle discretization. Then our low-rank approximation  $f = \sum_{i,j} U_i S_{ij} V_j$  becomes

$$F = USV^T, \quad \text{where } U \in \mathbb{R}^{n_x \cdot n_y \times r}, S \in \mathbb{R}^{r \times r}, V \in \mathbb{R}^{n_\phi \times r}.$$

The boundary data for  $x$  advection are then given by

$$F_L = K_L V_L^T, \quad \text{where } K_L \in \mathbb{R}^{n_y \times r_L}, V_L \in \mathbb{R}^{n_\phi \times r_L}$$

and

$$F_R = K_R V_R^T, \quad \text{where } K_R \in \mathbb{R}^{n_y \times r_R}, V_R \in \mathbb{R}^{n_\phi \times r_R}.$$

Note that  $r_L$  is the rank used on the left subdomain (i.e. on  $\Omega_L$ ) and  $r_R$  is the rank used on the right subdomain (i.e. on  $\Omega_R$ ). More details on the specific discretization that we use in the numerical results can be found in section 4.

In the following we will describe the augmentation procedure that we perform before Step 1 (i.e. the  $x$  advection step). A similar procedure is performed before step 2. It is clear (see figure

2) that only information coming from  $\partial\Omega_L$  and  $\partial\Omega_R$  is relevant. The augmentation procedure that we use is given in algorithm 4. The main idea is that we keep information from  $V_L$  and  $V_R$  as long as neglecting it would introduce an error larger than a user specified tolerance  $\text{tol}$  in the approximation space (i.e. the span of  $\hat{V}$ ). The output of the algorithm are new low-rank factors  $U^1$ ,  $S^1$  and  $V^1$  that, in general, have a higher rank, i.e. the resulting rank  $r_t$  satisfies  $r_t \geq r$ . We can then proceed with the  $x$  advection step according to algorithm 1 with the new low-rank factors. This, in particular, ensures that any boundary information can be represented at least to accuracy  $\text{tol}$ .

---

**Algorithm 4** Augmentation algorithm.

---

**Input:**  $U^0$ ,  $S^0$ ,  $V^0$  (such that  $F^0 = U^0 S^0 V^{0,T}$ ),  $S_L$ ,  $V_L$ ,  $S_R$ ,  $V_R$ , tolerance  $\text{tol}$

**Output:**  $U^1$ ,  $S^1$ ,  $V^1$  (such that  $F^1 = U^1 S^1 V^{1,T}$ )

- 1: Set  $L^0 = [V^0 S^{0,T}, V_L S_L^T, V_R S_R^T]$ .
- 2: Perform an SVD to obtain  $L^0 = \tilde{V} \tilde{\Sigma} \tilde{U}^T$ , where  $\tilde{V} \in \mathbb{R}^{n_\phi \times m}$ ,  $\tilde{\Sigma} \in \mathbb{R}^{m \times m}$  and  $\tilde{U} \in \mathbb{R}^{(r+r_L+r_R) \times m}$ .
- 3: According to some specified tolerance  $\text{tol}$ , calculate a truncated rank  $r_t$ : Choose  $r_t$  as the minimal number such that

$$\left( \sum_{j=r_t+1}^m \sigma_j^2 \right)^{\frac{1}{2}} \leq \text{tol},$$

where  $\sigma_j$  are the singular values in  $\tilde{\Sigma}$ . Additionally, impose  $r_t \geq r$ .

- 4: Truncate  $\tilde{V}$  to obtain  $\hat{V} = \tilde{V}(:, 1:r_t) \in \mathbb{R}^{n_\phi \times r_t}$ .
- 5: Extend our basis  $U^0$  with a random matrix  $U_{\text{rand}} \in \mathbb{R}^{n_x \cdot n_y \times (r_t-r)}$  and extend  $S^0$ , such that  $\hat{U} \hat{S} \hat{V}^T = U^0 S^0 V^{0,T} = F^0$  is satisfied, i.e.:

$$\hat{U} = [U^0, U_{\text{rand}}] \in \mathbb{R}^{n_x \cdot n_y \times r_t}, \quad \hat{S} = \begin{bmatrix} S^0 V^{0,T} \hat{V} \\ 0 \end{bmatrix} \in \mathbb{R}^{r_t \times r_t}.$$

- 6: Orthonormalize the new basis by performing a QR decomposition  $\hat{U} = U^1 S_U$  and  $\hat{V} = V^1 S_V$ . Also, set  $S^1 = S_U \hat{S} \hat{S}_V^T$ .

---

Let us note that there are two important differences compared to [24]. First, we obtain our augmented basis directly from the low-rank representation of the neighboring subdomains. That is, we do not need to form  $F_b$  (see step 1). This makes the algorithm computational more efficient. Second, we proceed with the computation by truncating  $L^0$ , which includes information of the  $V$  basis for both the current as well as the neighboring domains. This implies that in situations where the basis used for the neighboring domains is similar to the current one,  $r_t$  is only slightly larger than  $r$ . We will investigate this in more detail when discussing the numerical results.

Note that since the rank is increased in this step we have to truncate it at some point. Thus, after the advection in  $x$  and  $y$  we add a standard truncation step (see algorithm 5) that reduces the rank such that the error is below the user specified tolerance  $\text{tol}$ . This automatically results in a rank adaptive scheme, where the rank can increase and decrease depending on the properties of the solution.

---

**Algorithm 5** Truncation algorithm.

---

**Input:**  $U^0, S^0, V^0$  (such that  $F^0 = U^0 S^0 V^{0,T}$ ), tolerance tol

**Output:**  $U^1, S^1, V^1$  (such that  $F^1 = U^1 S^1 V^{1,T}$ )

- 1: Perform an SVD to obtain  $S^0 = \tilde{U} \tilde{\Sigma} \tilde{V}^T$ , where  $\tilde{U}, \tilde{V} \in \mathbb{R}^{r \times r}$  are orthonormal and  $\tilde{\Sigma} \in \mathbb{R}^{r \times r}$  is diagonal with descending singular values.
- 2: According to some specified tolerance tol, calculate a truncated rank  $r'$ : Choose  $r'$  as the minimal number such that

$$\left( \sum_{j=r'+1}^r \sigma_j^2 \right)^{1/2} \leq \text{tol},$$

where  $\sigma_j$  are the singular values in  $\tilde{\Sigma}$ .

Then, set  $\bar{U} = \tilde{U}(:, 1:r')$ ,  $\bar{V} = \tilde{V}(:, 1:r')$  and  $S^1 = \tilde{\Sigma}(1:r', 1:r')$ .

- 3: Update the basis as:

$$U^1 = U^0 \bar{U} \in \mathbb{R}^{n_x \cdot n_y \times r'}, \quad V^1 = V^0 \bar{V} \in \mathbb{R}^{n_\phi \times r'}.$$

---

### 3.5 Complete domain decomposition dynamical low-rank algorithm

Putting all the building blocks developed in the previous sections together we arrive at our domain decomposition low-rank algorithm that is detailed in algorithm 6.

---

**Algorithm 6** Domain decomposition low-rank algorithm.

---

**Input:** Low rank representation on each domain, tolerance tol

**Output:** Low rank representation on each domain

- 1: Add basis functions according to some tolerance tol and algorithm 4.
- 2: Run algorithm 1 to solve  $x$  advection.
- 3: Remove basis functions according to some tolerance tol and algorithm 5.
- 4: Add basis functions for inflowing values in  $y$  direction according to some tolerance tol, similar to algorithm 4.
- 5: Run algorithm 2 to solve  $y$  advection.
- 6: Remove basis functions according to some tolerance tol and algorithm 5.
- 7: Run algorithm 3 to solve absorption, scattering and the source term.

Note: This procedure is performed on each domain and repeated for every time step.

---

## 4 Numerical results

In this section we consider several well known test cases of the radiative transfer equation in order to demonstrate the effectiveness of the proposed method. We compare the proposed algorithm 6 with a standard dynamical low-rank approach that does not make use of domain decomposition. We first study a classic lattice and Hohlraum problem and show that our algorithm is more efficient than the classic low-rank approach. We then study a point source problem, where the rank on some part of the domain needs to be large in order to obtain an accurate solution. This example shows that the low-rank domain decomposition algorithm

can work efficiently in situations where classic low-rank methods require large memory and computational effort. The source code necessary to reproduce the numerical experiments can be found in [2].

All simulations conducted here use the classic Runge–Kutta method of order four (RK4) to perform the time integration. For the spatial discretization an upwind scheme is used. This is, in particular, necessary for the problems described here as the discontinuous interface between cells can otherwise lead to unphysical oscillations. For more details we refer to appendix A.

## 4.1 Lattice test problem

Our first problem is the lattice test case that has often been considered in the literature (see, e.g., [3, 29, 32, 5]). It is based on the blocks of a nuclear reactor core that has both highly absorbing and scattering regions. Our setup can be seen in figure 3. The full domain is one centimeter wide, i.e.  $x \in [0, 1]$  and  $y \in [0, 1]$ . For the angle we have  $\phi \in [0, 2\pi]$ . The spatial domain is then split up into a grid containing  $7 \times 7$  blocks. We choose our unit system such that  $c_{\text{adv}} = 1$ . The choice of the other coefficients can be seen in figure 3. The red blocks describe a highly absorbing material with  $c_s = 0$  and  $c_t = 10$ , while the blue blocks describe a material that scatters but has no absorption ( $c_s = 1$  and  $c_t = 1$ ). The right of figure 3 describes the source  $Q(x, y)$ . For the yellow block we have  $Q(x, y) = 1$ , while in the remainder of the domain we set  $Q(x, y) = 0$ . The initial condition is  $f(t = 0, x, y, \phi) = 10^{-9}$ .

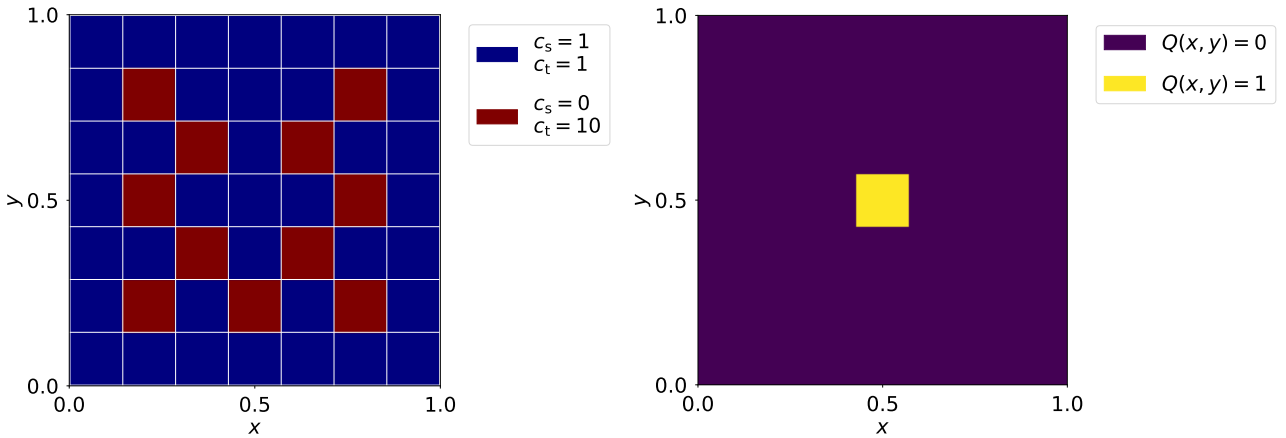


Figure 3: Setup of the lattice test problem.

We compare our domain decomposition approach to a classic dynamical low-rank algorithm (i.e. without domain decomposition). The grid is discretized equidistantly, such that we have 252 grid points in  $x$ ,  $y$  and  $\phi$ . The time step is chosen to be  $\Delta t = 0.5 \cdot \Delta x$ . On the boundary we have an outflow boundary condition. The density  $\rho$  for times  $t = 0.3$ ,  $t = 0.5$  and  $t = 0.7$  is shown on the left-hand side of figure 4. As expected, the radiation induced by the source term spreads outwards, moving around the absorbing blocks. A tolerance  $\text{tol} = 3 \cdot 10^{-5}$ , which is used to perform rank adaptivity, is used in these simulations.

We compare this with our proposed domain decomposition approach which is shown on the right of figure 4. The plots agree well. The tolerance used for the rank-adaptivity of the domain decomposition low-rank simulation is  $\text{tol} = 6 \cdot 10^{-6}$ . This yields a similar error for both methods. Comparing to a reference solution  $f_{\text{ref}}$  that has been computed with the classic

low-rank method without domain decomposition and  $\text{tol} = 10^{-10}$ , we get

$$\|f - f_{\text{ref}}\| := \frac{\|f - f_{\text{ref}}\|_{L^2}}{\|1\|_{L^2}} \approx 1.12 \cdot 10^{-4}.$$

The error of the low-rank method without domain decomposition is approximately  $1.13 \cdot 10^{-4}$  (compared to the same reference solution). Note that we have chosen the tolerance in the simulations such that we get roughly the same overall error. This required the choice of different tolerances for the two methods. Note that for the classic dynamical low-rank scheme we use a different approach to achieve rank adaptivity (as there is no inflow in this case), which can be found in [23].

We now compare the ranks that are required to obtain the described results. For the low-rank method without domain decomposition the rank as a function of time is given in figure 5. As expected, the rank increases steadily over time. The highest rank required is 46 at the end of our simulation. For the domain decomposition approach the rank is different in each block. The ranks in each block as a function of time is shown in figure 6. Here we have to distinguish between the rank required to store our solution (bottom of the plot; this would be the approximation that is written to disk) and the highest rank that occurs during the computation, also called intermediate rank (top of the plot; this is the rank that determines the amount of memory required to run the simulation).

We note that only in a single block the rank required by the domain decomposition low-rank method is as large as what is required for the classic low-rank method. In most other blocks the rank required is significantly lower. This is because the low-rank representation only needs to resolve a more localized region of space. Moreover, in some blocks the solution is naturally low-rank (e.g. due to strong absorption or because not much is happening in that block at early times of the simulation). Thus, the domain decomposition approach reduces the number of degrees of freedom required to run the simulation significantly. This is shown in figure 7, where we see roughly a factor of 2.2 reduction when comparing maximum memory usage (i.e. we compare with the intermediate rank, given by the dotted line) and roughly a factor of five less memory to store the solution (i.e. we compare with the rank obtained after each time step, given by the full line).

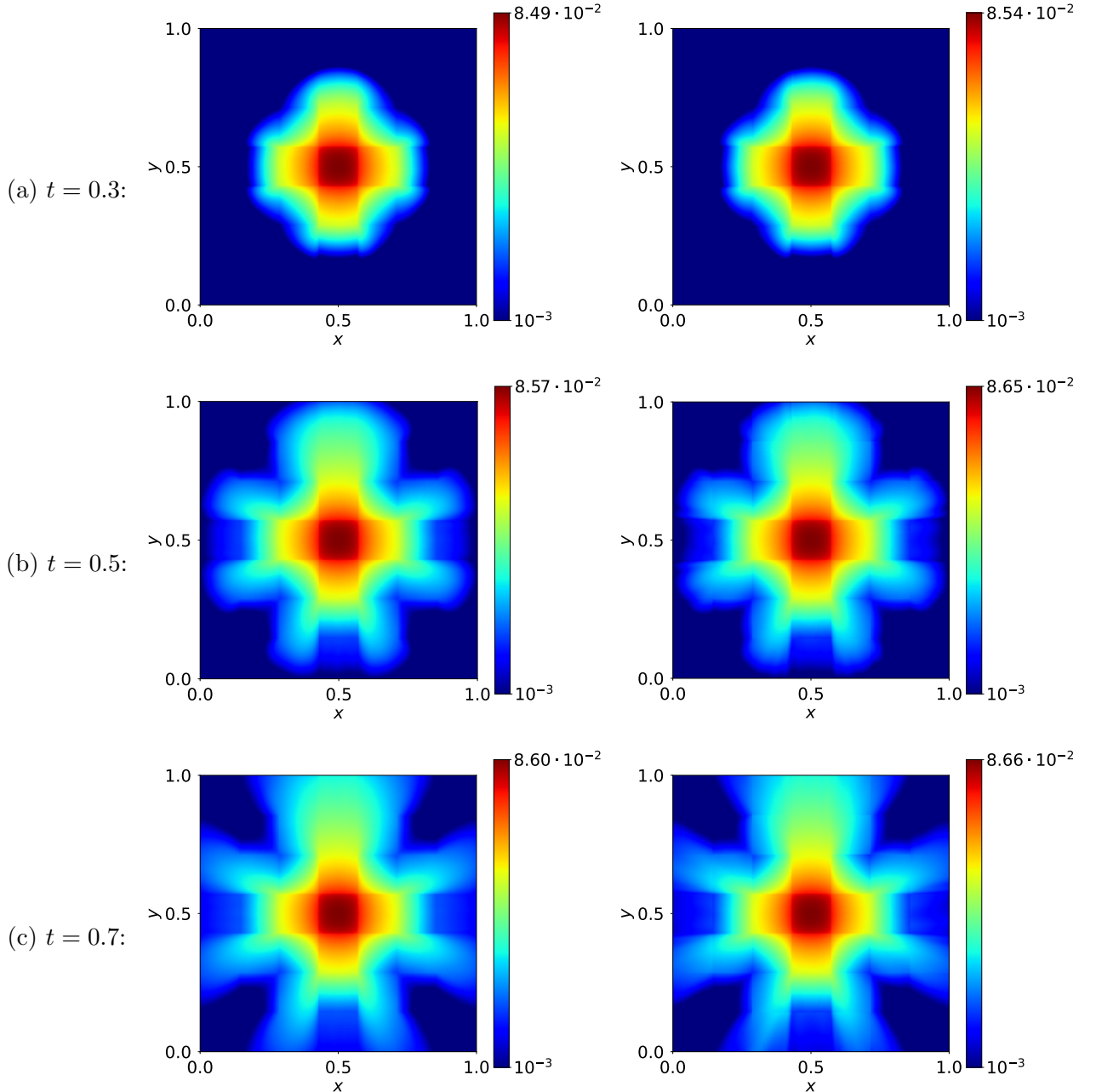


Figure 4: We show  $\rho(t, x, y)$  obtained by solving the lattice test problem with a classic dynamical low-rank algorithm (i.e. with a single low-rank representation for the entire domain) on the left and with the domain decomposition low-rank algorithm 6 on the right. For the latter,  $7 \times 7$  subdomains, each containing 36 grid points in both the  $x$  and  $y$  directions, have been used.

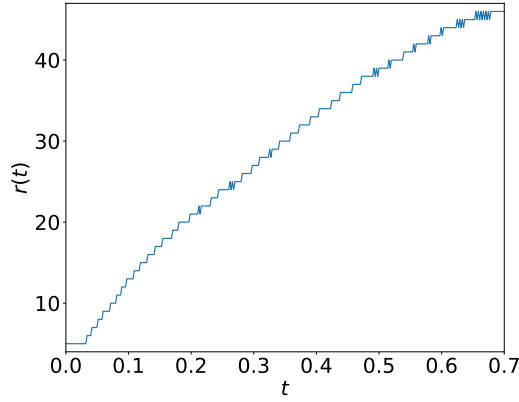


Figure 5: We show the time evolution of the rank for the classic low-rank simulation of the lattice test problem. As an adaptive rank scheme we used the scheme described in [23] with  $\text{tol} = 3 \cdot 10^{-5}$ .

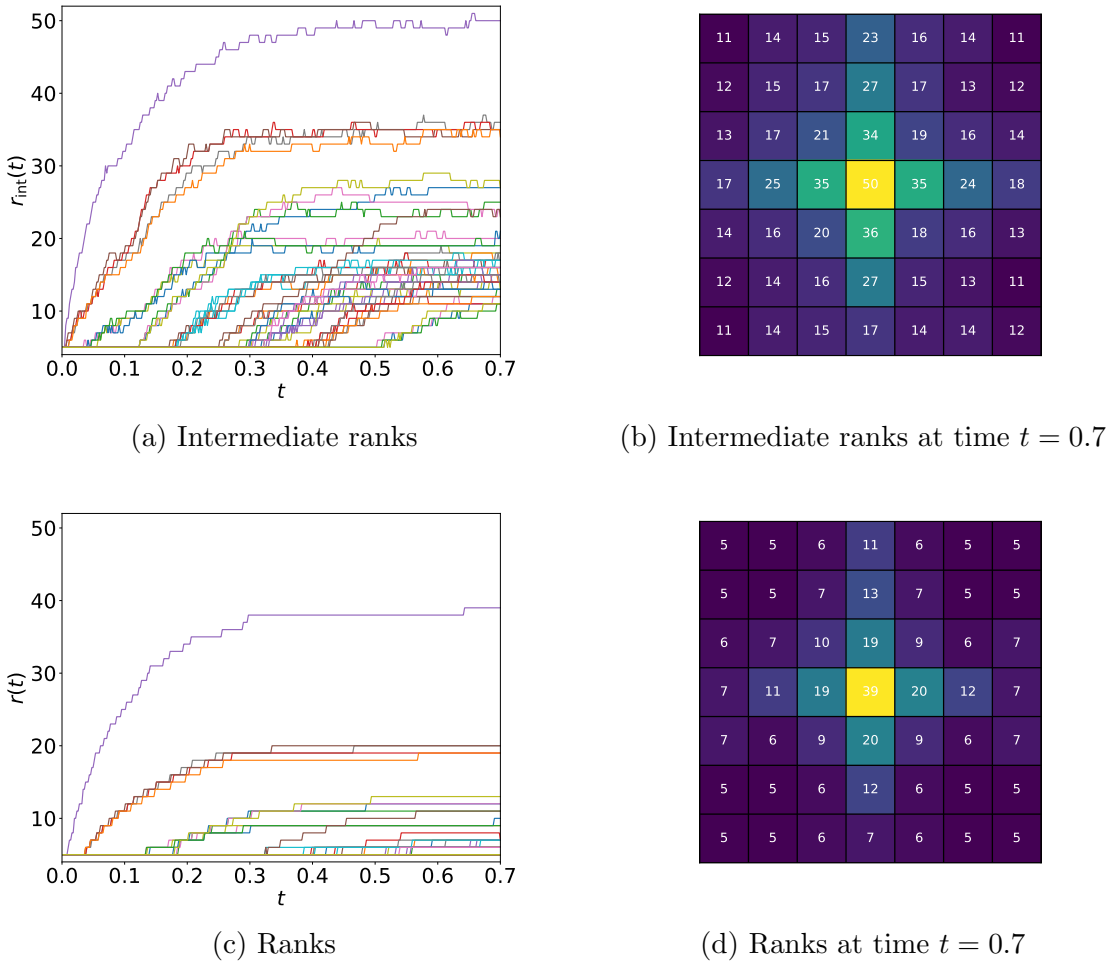


Figure 6: We show the time evolution of the intermediate ranks and ranks after the time step for the domain decomposition dynamical low-rank simulation of the lattice test problem. The adaptive rank scheme as proposed in algorithms 4 and 5 with  $\text{tol} = 6 \cdot 10^{-6}$  was used.

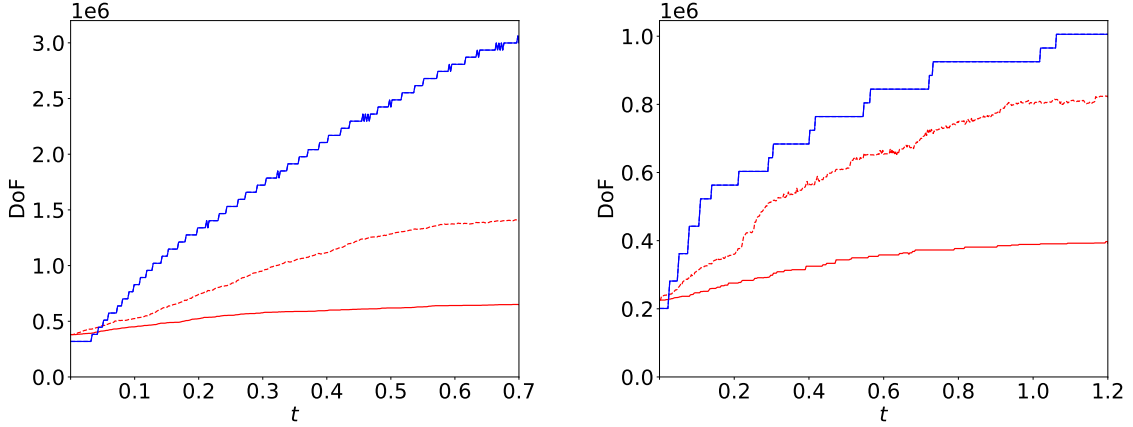


Figure 7: We show degrees of freedom (DoF) as a function of time for the low-rank simulation of the lattice test problem (left) and the Hohlraum test problem (right) for the classic low-rank method (blue) and the domain decomposition low-rank method (algorithm 6) (red).

## 4.2 Hohlraum test problem

The second test case we consider is a hohlraum simulation (see, e.g., [32, 3, 29]). The motivation for this test case comes from inertial confinement fusion, where the hohlraum holds a small capsule of fusion fuel. In our case, we look at a simplified 2-dimensional version of a hohlraum. As can be seen in figure 8, we have a rectangular domain 1 cm wide in the  $x$  and  $y$  directions. The angular domain is again  $\phi \in [0, 2\pi]$ . The advection coefficient is equal to 1 on the whole domain. The blue blocks describe a vacuum, where  $c_t = 0$  and  $c_s = 0$ , while the red blocks describe a strongly absorbing material with  $c_t = 100$  and  $c_s = 0$ .

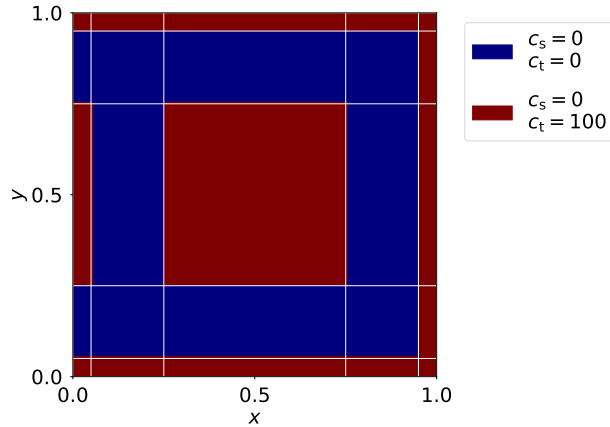


Figure 8: Setup of the Hohlraum and point source test problem.

In this problem there is no source, i.e.  $Q(x, y) = 0$ . Radiation enters via an inflow boundary condition given by

$$f(t, x = 0, y, \phi) = 1, \text{ for all } t \in \mathbb{R}^+, y \in [0, 1] \text{ and } \phi \in \left[0, \frac{\pi}{2}\right] \cup \left[\frac{3\pi}{2}, 2\pi\right].$$

At all other boundaries in the domain we have either a zero-inflow condition or an outflow boundary. The initial condition is again given by  $f(t = 0, x, y, \phi) = 10^{-9}$ .

We again compare the low-rank methods with and without domain decomposition. An equidistant grid with 200 grid points in  $x$ ,  $y$  and  $\phi$  is used, and the time step size is set to  $\Delta t = 0.5 \cdot \Delta x$ . The results for  $\rho(t, x, y)$  at times  $t = 0.2$ ,  $t = 0.4$  and  $t = 1.2$  are shown in figure 9 (left without domain decomposition and right with domain decomposition). We observe that the radiation enters the domain on the left boundary and moves through the vacuum. The absorbing blocks prevent radiation to move through the material and instead force it around. Similar results are observed for the low-rank method with and without domain decomposition.

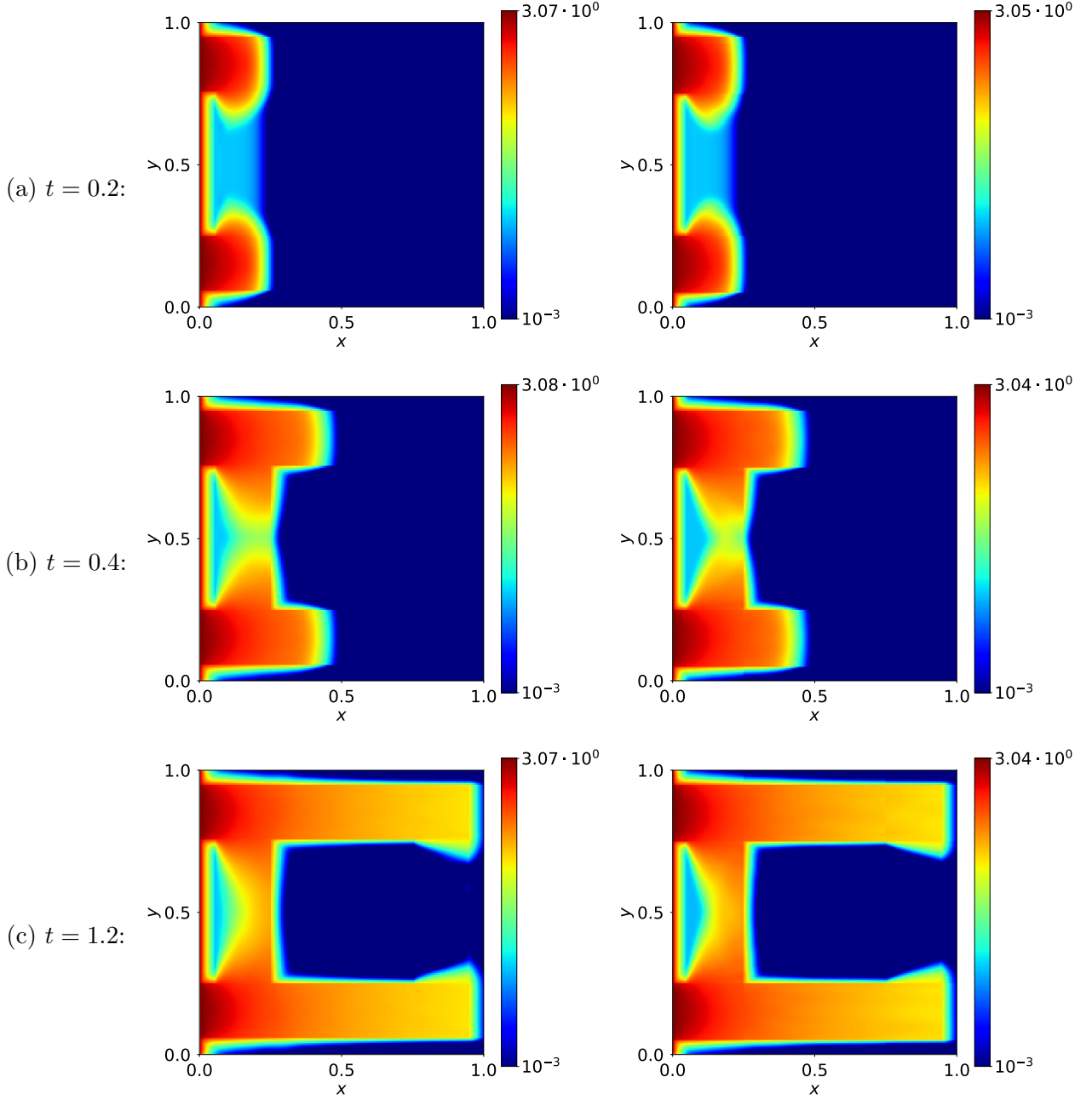


Figure 9: We show  $\rho(t, x, y)$  obtained by solving the Hohlraum test problem with the classic dynamical low-rank algorithm (left) and with the domain decomposition low-rank algorithm 6 (right). For the latter, the grid is divided into  $5 \times 5$  subdomains.

We again compare the time evolution of the ranks for the approach without (figure 10) and with domain decomposition (figure 11). We note that we have chosen a tolerance of  $\text{tol} = 10^{-4}$

for the classic dynamical low-rank approach. This is necessary to avoid visible artifacts in the numerical solution. For the domain decomposition low-rank approach a tolerance of  $\text{tol} = 10^{-3}$  is sufficient to obtain good results. We note, however, that the largest intermediate rank of the domain decomposition low-rank algorithm is roughly the same in both cases as is the error compared to a reference solution computed with the classic method and  $\text{tol} = 10^{-10}$  ( $\|f - f_{\text{ref}}\| \approx 1.3 \cdot 10^{-2}$  for the classic DLRA approach and  $\|f - f_{\text{ref}}\| \approx 2.5 \cdot 10^{-2}$  for the domain decomposition). We believe that the slightly larger error in case of the domain decomposition is actually not a low-rank error, but a time discretization error caused by freezing the boundary condition in time.

Comparing the degrees of freedom required by each method in figure 7 on the right we see that the domain decomposition approach requires roughly 20 % less degrees of freedom when comparing maximum memory usage (i.e. we compare with the intermediate rank) and more than a factor of two less memory to store the solution (i.e. we compare with the rank obtained after the time step). This is despite the fact that both methods have a similar maximal rank. However, for the domain decomposition approach a significantly smaller rank is used in most subdomains.

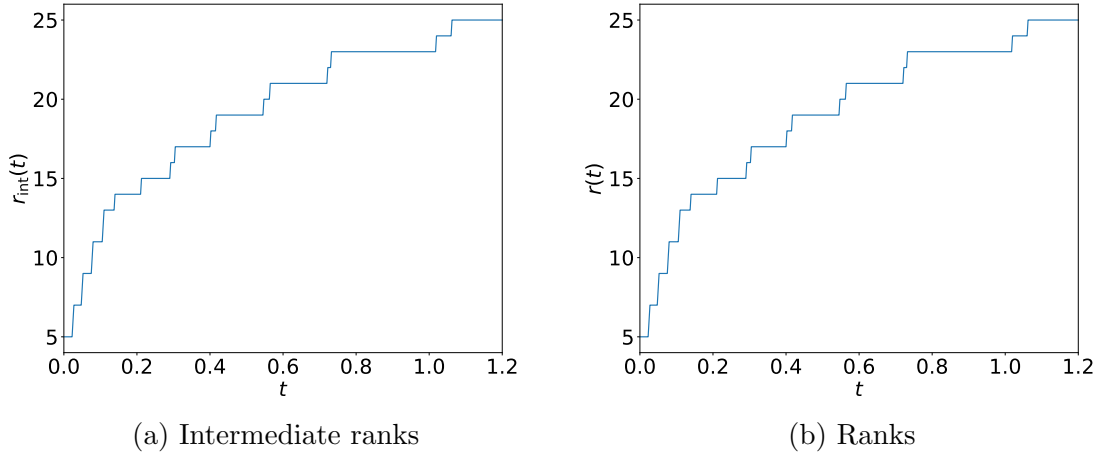
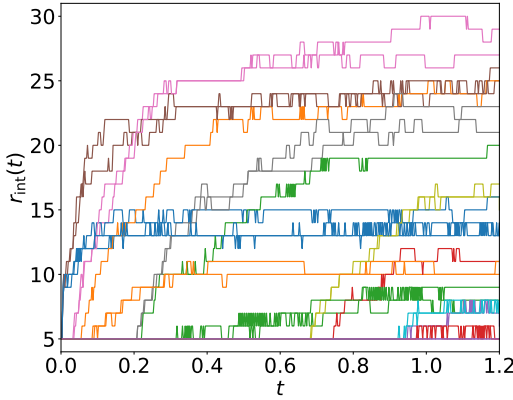
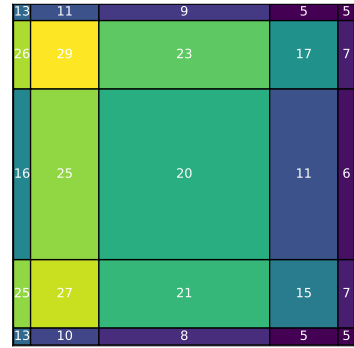


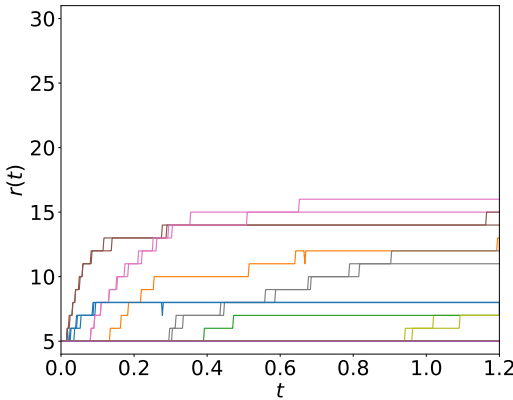
Figure 10: We show the time evolution of the intermediate rank and rank after the time step for the classic low-rank simulation of the Hohlraum test problem. As an adaptive rank scheme we used the scheme as proposed in algorithms 4 and 5 with  $\text{tol} = 10^{-4}$ .



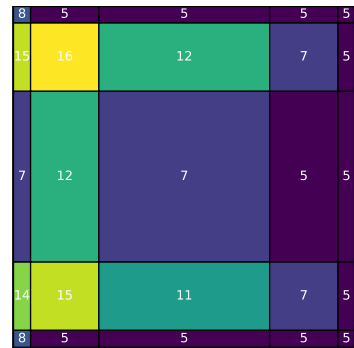
(a) Intermediate ranks



(b) Intermediate ranks at time  $t = 1.2$



(c) Ranks



(d) Ranks at time  $t = 1.2$

Figure 11: We show the time evolution of the intermediate ranks and ranks after the time step for the domain decomposition dynamical low-rank simulation of the Hohlraum test problem. The adaptive rank scheme as proposed in algorithms 4 and 5 with  $\text{tol} = 10^{-3}$  was used.

### 4.3 Isotropic point source test problem

The final test case we consider is a simulation with an isotropic point source. It is well known that an isotropic point source propagating into vacuum can only be approximated well by using a large rank. We use the same setup as in the Hohlraum example from section 4.2, but instead of having a uniform inflow on the entire left boundary, we now place a point source on the left boundary, i.e.

$$f(t, x = 0, y, \phi) = \frac{1}{\sqrt{2\pi}\sigma} \exp\left(-\frac{(y - y_0)^2}{2\sigma^2}\right), \text{ for all } t \in \mathbb{R}^+, y \in [0, 1] \\ \text{and } \phi \in \left[0, \frac{\pi}{2}\right] \cup \left[\frac{3\pi}{2}, 2\pi\right],$$

where  $y_0 = 0.85$  and a small  $\sigma = 10^{-2}$ . To resolve the point source accurately, we require 600 grid points in both the  $x$  and  $y$  directions. We still use 200 grid points in  $\phi$ .

The results for the classic low-rank method and the proposed domain decomposition low-rank algorithm 6 for  $\rho(t, x, y)$  at times  $t = 0.3$ ,  $t = 0.7$ , and  $t = 1.0$  are shown in figure 12. As

can be clearly observed, the radiation enters our domain on the upper left side of the boundary and propagates into the domain. We chose our tolerances, such that we get identical results for both simulations.

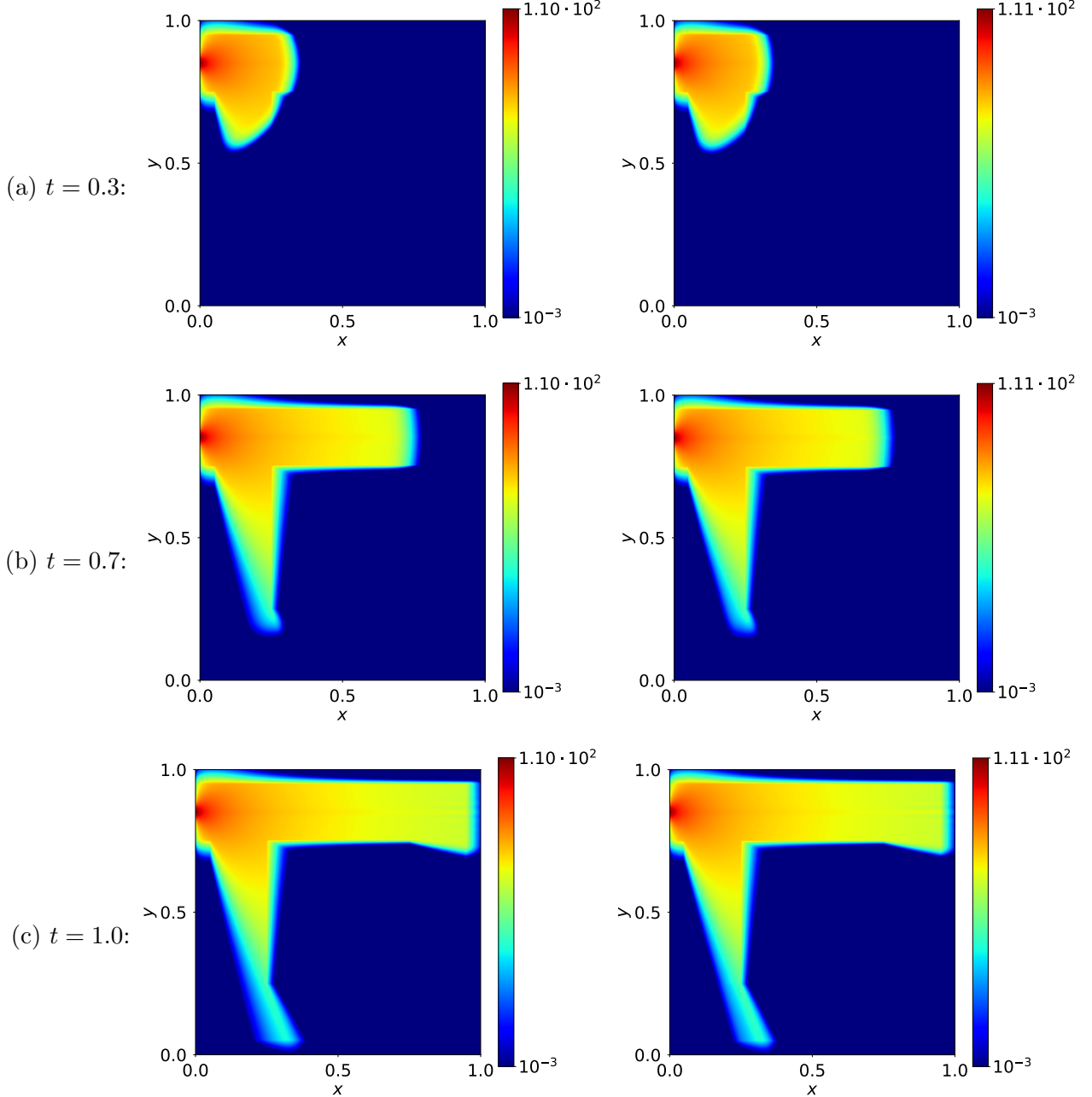


Figure 12: We show  $\rho(t, x, y)$  obtained by solving the point source test problem with the classic dynamical low-rank algorithm (left) and with the domain decomposition low-rank algorithm 6 (right). For the latter, the grid is divided into  $5 \times 5$  subdomains.

Here, we really want to focus on the ranks required by each method and compare the degrees of freedom. The ranks as a function of time for the two configurations are shown in figures 13 and 14, respectively. While for classic simulations the rank needs to be high on the full domain, for domain decomposition simulations one can clearly see that even though the rank that is required close to the point source is high, as the radiation spreads into the domain a significantly lower rank can be used.

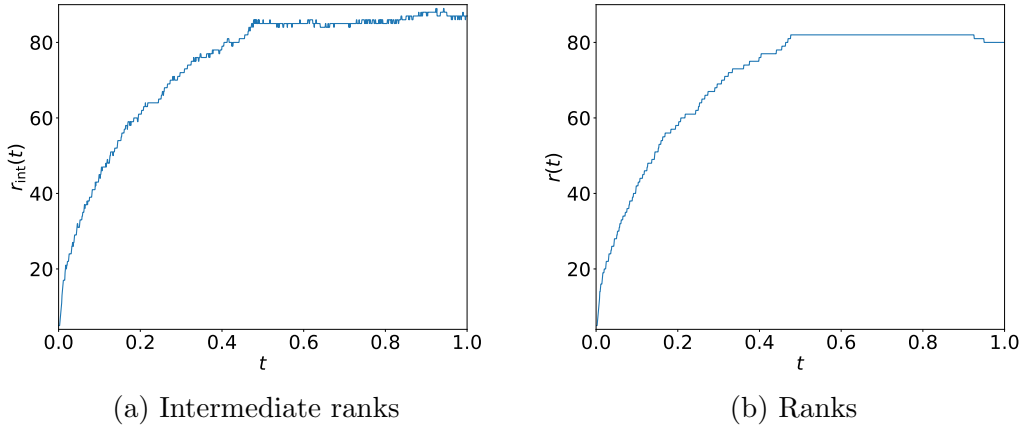


Figure 13: We show the time evolution of the intermediate rank and rank after the time step for the classic low-rank simulation of the point source test problem. As an adaptive rank scheme we used the scheme as proposed in algorithms 4 and 5 with  $\text{tol} = 10^{-5}$ .

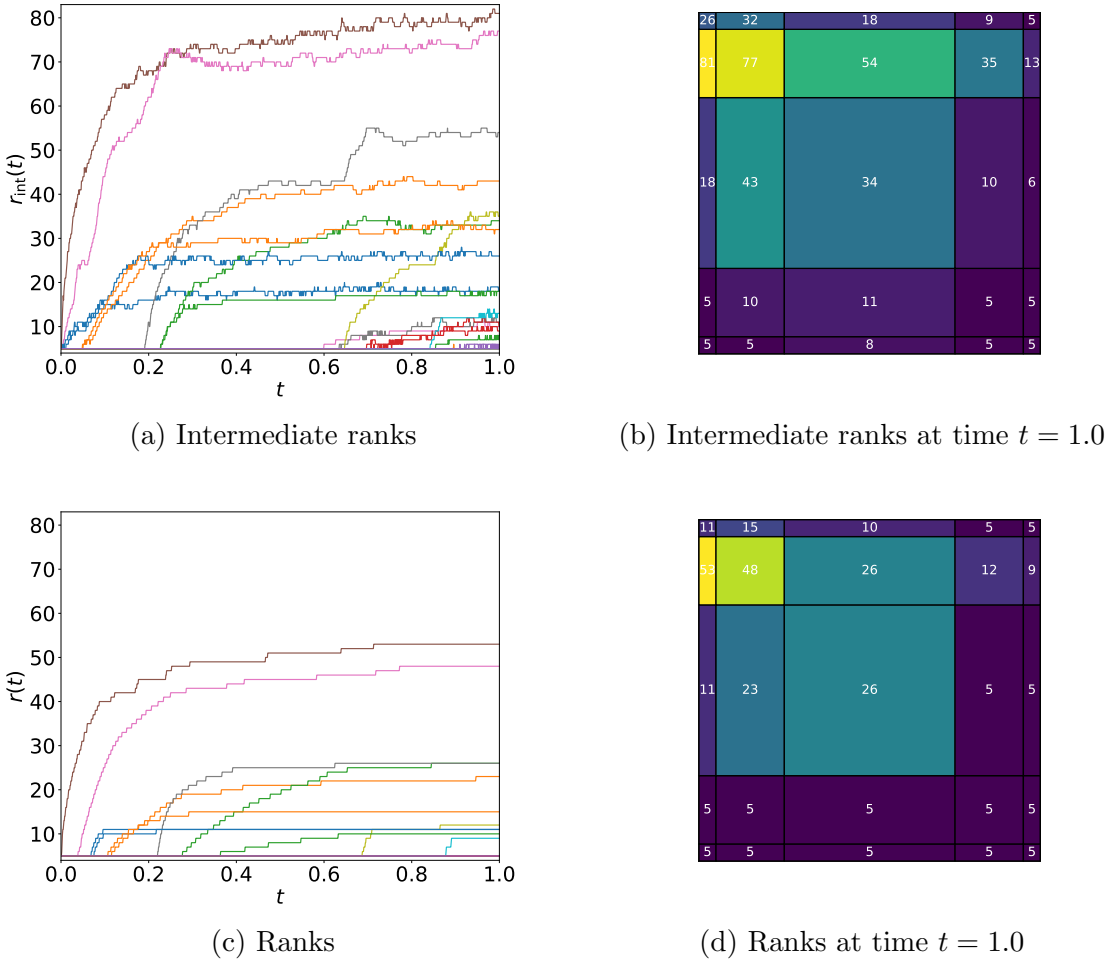


Figure 14: We show the time evolution of the intermediate ranks and ranks after the time step for the domain decomposition dynamical low-rank simulation of the point source test problem. The adaptive rank scheme as proposed in algorithms 4 and 5 with  $\text{tol} = 10^{-4}$  was used.

Thus, the domain decomposition approach here has the clear advantage that the overall degrees of freedom can be kept significantly lower (roughly by a factor of 3 for the intermediate rank and 5 for the rank after each time step) compared to a classic low-rank approach, as can be seen in figure 15.

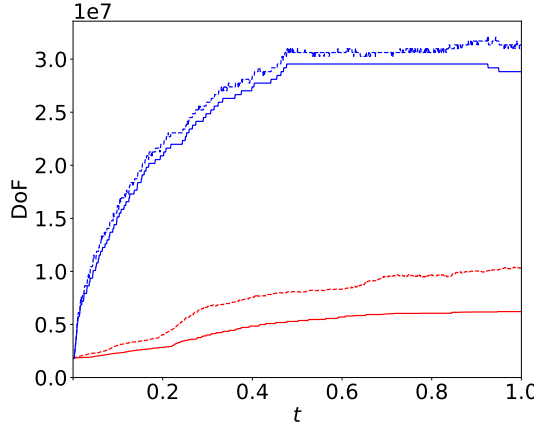


Figure 15: We show degrees of freedom (DoF) as a function of time for the low-rank simulation of the point source test problem for the classic low-rank method (blue) and the domain decomposition low-rank method (algorithm 6) (red).

## 5 Acknowledgements

This work was performed under the auspices of the U.S. Department of Energy by Lawrence Livermore National Laboratory under Contract DE-AC52-07NA27344.

## References

- [1] Lena Baumann et al. “Energy stable and conservative dynamical low-rank approximation for the Su-Olson problem”. In: *SIAM Journal on Scientific Computing* 46.2 (2024). DOI: 10.1137/23M1586215.
- [2] S. Brunner. *Domain-decomposition dynamical low-rank method for the radiative transfer equation*. <https://github.com/StefanBrunner2709/Domain-decomposition-dynamical-low-rank-method-for-the-radiative-transfer-equation.git>. 2025.
- [3] T.A. Brunner. “Forms of approximate radiation transport”. In: SAND2002-1778 (2002). URL: <https://www.osti.gov/servlets/purl/800993>.
- [4] F. Cassini and L. Einkemmer. “Efficient 6D Vlasov simulation using the dynamical low-rank framework Ensign”. In: *Comput. Phys. Commun.* 280 (2022), p. 108489. DOI: 10.1016/j.cpc.2022.108489.
- [5] G. Ceruti, J. Kusch, and C. Lubich. “A Parallel Rank-Adaptive Integrator for Dynamical Low-Rank Approximation”. In: *SIAM Journal on Scientific Computing* 46.3 (2024), B205–B228. DOI: 10.1137/23M1565103.
- [6] G. Ceruti, J. Kusch, and C. Lubich. “A rank-adaptive robust integrator for dynamical low-rank approximation”. In: *BIT Numerical Mathematics* 62.4 (2022). DOI: 10.1007/s10543-021-00907-7.

[7] G. Ceruti and C. Lubich. “An unconventional robust integrator for dynamical low-rank approximation”. In: *BIT Numerical Mathematics* 62.1 (2022), pp. 23–44. DOI: [10.1007/s10543-021-00873-0](https://doi.org/10.1007/s10543-021-00873-0).

[8] G. Ceruti et al. “A robust second-order low-rank BUG integrator based on the midpoint rule”. In: *BIT Numer. Math.* 64.3 (2024). DOI: [10.1007/s10543-024-01032-x](https://doi.org/10.1007/s10543-024-01032-x).

[9] C. Cheng and G. Knorr. “The integration of the Vlasov equation in configuration space”. In: *J. Comput. Phys.* 22 (1976), pp. 330–351. DOI: [10.1016/0021-9991\(76\)90053-X](https://doi.org/10.1016/0021-9991(76)90053-X).

[10] J. Coughlin, J. Hu, and U. Shumlak. “Robust and conservative dynamical low-rank methods for the Vlasov equation via a novel macro-micro decomposition”. In: *Journal of Computational Physics* 509 (2024), p. 113055. ISSN: 0021-9991. DOI: [10.1016/j.jcp.2024.113055](https://doi.org/10.1016/j.jcp.2024.113055).

[11] Z. Ding, L. Einkemmer, and Q. Li. “Dynamical Low-Rank Integrator for the Linear Boltzmann Equation: Error Analysis in the Diffusion Limit”. In: *SIAM J. Numer. Anal.* 59.4 (2021). DOI: [10.1137/20M1380788](https://doi.org/10.1137/20M1380788).

[12] L. Einkemmer. “A mixed precision semi-Lagrangian algorithm and its performance on accelerators”. In: *Proceedings of the 2016 International Conference on High Performance Computing & Simulation (HPCS)*. 2016, pp. 74–80. DOI: [10.48550/arXiv.1603.07008](https://doi.org/10.48550/arXiv.1603.07008).

[13] L. Einkemmer. “Accelerating the simulation of kinetic shear Alfvén waves with a dynamical low-rank approximation”. In: *J. Comput. Phys.* 501 (2024), p. 112757. DOI: [10.1016/j.jcp.2024.112757](https://doi.org/10.1016/j.jcp.2024.112757).

[14] L. Einkemmer, J. Hu, and J. Kusch. “Asymptotic-Preserving and Energy Stable Dynamical Low-Rank Approximation”. In: *SIAM Journal on Numerical Analysis* 62.1 (2024), pp. 73–92. ISSN: 1095-7170. DOI: [10.1137/23m1547603](https://doi.org/10.1137/23m1547603).

[15] L. Einkemmer, J. Hu, and Y. Wang. “An asymptotic-preserving dynamical low-rank method for the multi-scale multi-dimensional linear transport equation”. In: *J. Comput. Phys.* 439 (2021). DOI: <https://doi.org/10.1016/j.jcp.2021.110353>.

[16] L. Einkemmer and I. Joseph. “A mass, momentum, and energy conservative dynamical low-rank scheme for the Vlasov equation”. In: *J. Comput. Phys.* 443 (2021), p. 110495. DOI: [10.1016/j.jcp.2021.110495](https://doi.org/10.1016/j.jcp.2021.110495).

[17] L. Einkemmer, J. Kusch, and S. Schotthöfer. “Construction of high-order conservative basis-update and Galerkin dynamical low-rank integrators”. In: *arXiv:2311.06399* (Nov. 2023). DOI: [10.48550/ARXIV.2311.06399](https://doi.org/10.48550/ARXIV.2311.06399). arXiv: 2311.06399 [math.NA].

[18] L. Einkemmer and C. Lubich. “A Low-Rank Projector-Splitting Integrator for the Vlasov-Poisson Equation”. In: *SIAM Journal on Scientific Computing* 40.5 (2018), B1330–B1360. DOI: [10.1137/18M116383X](https://doi.org/10.1137/18M116383X).

[19] L. Einkemmer et al. “A review of low-rank methods for time-dependent kinetic simulations”. In: *J. Comput. Phys.* 538 (Oct. 2025), p. 114191. ISSN: 0021-9991. DOI: [10.1016/j.jcp.2025.114191](https://doi.org/10.1016/j.jcp.2025.114191).

[20] Martin Frank, Jonas Kusch, and Chinmay Patwardhan. “Asymptotic-Preserving and Energy Stable Dynamical Low-Rank Approximation for Thermal Radiative Transfer Equations”. In: *Multiscale Modeling & Simulation* 23.1 (2025), pp. 278–312. DOI: [10.1137/24M1646303](https://doi.org/10.1137/24M1646303).

[21] W. Guo, J. Ferdous Ema, and J.-M. Qiu. “A local Macroscopic Conservative (LoMaC) Low Rank Tensor Method with the Discontinuous Galerkin Method for the Vlasov Dynamics”. In: *Commun. Appl. Math. Comput.* 6.1 (2024), pp. 550–575. DOI: [10.1007/s10915-024-02684-1](https://doi.org/10.1007/s10915-024-02684-1).

[22] E. Hairer, C. Lubich, and G. Wanner. *Geometric numerical integration: structure-preserving algorithms for ordinary differential equations*. Springer, 2006.

- [23] M. Hochbruck, M. Neher, and S. Schrammer. “Rank-adaptive dynamical low-rank integrators for first-order and second-order matrix differential equations”. In: *BIT Numerical Mathematics* 63 (2023). DOI: 10.1007/s10543-023-00942-6.
- [24] J. Hu and Y. Wang. “An Adaptive Dynamical Low Rank Method for the Nonlinear Boltzmann Equation”. In: *Journal of Scientific Computing* 92.2 (2022). DOI: 10.1007/s10915-022-01934-4.
- [25] O. Koch and C. Lubich. “Dynamical Low-Rank Approximation”. In: *SIAM J. Matrix Anal. Appl.* 29 (2007), pp. 434–454. DOI: 10.1137/050639703.
- [26] J. Kusch and P. Stammer. “A robust collision source method for rank adaptive dynamical low-rank approximation in radiation therapy”. In: *ESAIM: Mathematical Modelling and Numerical Analysis* 57.2 (2023), pp. 865–891. DOI: 10.1051/m2an/2022090.
- [27] J. Kusch et al. “Dynamical low-rank approximation for Burgers’ equation with uncertainty”. In: *Int. J. Uncertain. Quantif.* 12.5 (2022), pp. 1–21. DOI: 10.1615/int.j.uncertaintyquantification.2022039345.
- [28] C. Lubich and I. V. Oseledets. “A projector-splitting integrator for dynamical low-rank approximation”. In: *BIT Numerical Mathematics* 54.1 (2014), pp. 171–188. DOI: 10.1007/s10543-013-0454-0.
- [29] R. G. McClarren and C. D. Hauck. “Robust and accurate filtered spherical harmonics expansions for radiative transfer”. In: *Journal of Computational Physics* 229.16 (2010), pp. 5597–5614. ISSN: 0021-9991. DOI: <https://doi.org/10.1016/j.jcp.2010.03.043>.
- [30] Z. Peng and R. McClarren. “A high-order/low-order (HOLO) algorithm for preserving conservation in time-dependent low-rank transport calculations”. In: *J. Comput. Phys.* 447.110672 (2021). DOI: 10.1016/j.jcp.2021.110672.
- [31] Z. Peng, R. McClarren, and M. Frank. “A low-rank method for two-dimensional time-dependent radiation transport calculations”. In: *J. Comput. Phys.* 421.109735 (2020). DOI: 10.1016/j.jcp.2020.109735.
- [32] Z. Peng and R. G. McClarren. “A sweep-based low-rank method for the discrete ordinate transport equation”. In: *Journal of Computational Physics* 473 (2023), p. 111748. ISSN: 0021-9991. DOI: <https://doi.org/10.1016/j.jcp.2022.111748>.
- [33] C. Scalone et al. “A multi-fidelity adaptive dynamical low-rank based optimization algorithm for fission criticality problems”. In: *Journal of Scientific Computing* (2025). DOI: 10.1007/s10915-025-02907-z.
- [34] E. Sonnendrücker et al. “The semi-Lagrangian method for the numerical resolution of the Vlasov equation”. In: *J. Comput. Phys.* 149.2 (1999), pp. 201–220. DOI: 10.1006/jcph.1998.6148.

## A Application of upwind discretization to algorithm 6

Our goal in this section is to apply the first order upwind scheme to the K step in both algorithms 1 and 2. We will only show the derivation for the  $x$  advection step, since the  $y$  advection step can be done analogously.

To begin, we will rewrite equation (17) in a discretized setting using matrices in linear algebra notation. We get

$$\partial_t K = -c_{\text{adv}} D_X K C, \quad (27)$$

where  $C = V^T \text{diag}(\sin(\phi))V \cdot \Delta\phi$  and  $D_X$  is the discretization of  $\partial_x$ . In order to obtain the direction of flow we diagonalize the symmetric and small matrix  $C$ . This gives

$$C = P\Lambda P^{-1},$$

where  $\Lambda$  is a diagonal matrix with eigenvalues on its diagonal and  $P$  contains the corresponding eigenvectors. Plugging this into equation (27) we get

$$\partial_t K = -c_{\text{adv}} D_X K P \Lambda P^{-1}.$$

Next, we express  $D_X K P$  by applying the upwind matrices  $D_X^-$  and  $D_X^+$  to each column of  $K P$ , depending on the sign of the corresponding eigenvalue in  $\Lambda$ . More precisely, if  $\Lambda[i, i] > 0$ , then

$$D_X K P[:, i] = D_X^- K P[:, i],$$

and if  $\Lambda[i, i] < 0$ , then

$$D_X K P[:, i] = D_X^+ K P[:, i].$$